Reversible Self-Replication of Spatiotemporal Kerr Cavity Patterns

Salim B. Ivars,[1,2,3] Yaroslav V. Kartashov,[2,4] Lluis Torner,[2,5] J. Alberto Conejero,[1] and Carles Milián[1,2,*]
[1]Institut Universitari de Matemàtica Pura i Aplicada, Universitat Politècnica de València, 46022 València, Spain
[2]ICFO—Institut de Ciències Fotòniques, The Barcelona Institute of Science and Technology, 08860 Castelldefels (Barcelona), Spain
[3]Departament de Física, Universitat Politècnica de Catalunya, 08222 Terrassa (Barcelona), Spain
[4]Institute of Spectroscopy, Russian Academy of Sciences, Troitsk, Moscow, 108840, Russia
[5]Universitat Politècnica de Catalunya, 08034 Barcelona, Spain

(Received 16 August 2020; accepted 13 January 2021; published 12 February 2021)

We uncover a novel and robust phenomenon that causes the gradual self-replication of spatiotemporal Kerr cavity patterns in cylindrical microresonators. These patterns are inherently synchronized multifrequency combs. Under proper conditions, the axially localized nature of the patterns leads to a fundamental drift instability that induces transitions among patterns with a different number of rows. Self-replications, thus, result in the stepwise addition or removal of individual combs along the cylinder's axis. Transitions occur in a fully reversible and, consequently, deterministic way. The phenomenon puts forward a novel paradigm for Kerr frequency comb formation and reveals important insights into the physics of multidimensional nonlinear patterns.

DOI: 10.1103/PhysRevLett.126.063903

The demonstration of a microresonator temporal soliton [1] and its subsequent stabilization [2,3] yielded and strongly boosted a wide range of applications of the associated stable frequency combs, such as frequency synthesis [4], spectroscopy [5], communications [6], and ranging [7], among many others (see, e.g., Refs. [8–10] for reviews). Aside from the widely employed single-soliton states, the interest in other nonlinear waves such as Turing rolls is also growing rapidly, as these waves are also very useful and may result in more efficient frequency comb generation [11–17]. Nevertheless, ongoing research on microresonator frequency combs remains strongly focused on essentially one-dimensional geometries, while potential advantages or qualitatively new ways to control and manipulate combs in multidimensional cavity geometries are not yet clearly identified.

In this Letter, we show that cylindrical Kerr microresonators, the natural two-dimensional extension of microrings [see Fig. 1(a)], offer a remarkably robust mechanism to replicate and erase frequency combs along the axial direction. Each comb corresponds to a row of a spatiotemporal hexagonal pattern constituted by a periodic arrangement of solitonic pulses, so that the N-row spatiotemporal patterns localized along the axial direction are regarded as N-frequency comb states (cf. Fig. 1). Individual combs are added or removed one by one in a stepwise deterministic way solely by tuning the width of the external laser pump beam. A powerful feature of the multicomb states introduced here is that all combs tend to be identical to each other; thus, matching among their free spectral range (FSR) occurs naturally, a property that is of great importance in the areas of high-precision dual-comb spectroscopy [18], ultrafast communications [6], and radio-frequency (rf) links [19]. In addition, such combs are inherently synchronized, which is fundamentally attractive [20] and may be beneficial for imaging applications requiring many combs [21]. In practice, multifrequency comb states may be realized with microrods [22], pumped from rectangular waveguide or flattened fibers, or integrated microcylinders [23] coupled to integrated waveguides.

From a fundamental standpoint, the effect uncovered here is related to the phenomenon of pattern self-replication, which typically manifests as spot multiplications in reaction-diffusion systems [24–26] or pattern expansions in thermoconvection [27]. Self-replications include the symmetry-preserving transformations occurring within a given pattern family, as is the case here, in contrast to symmetry transformations, widely studied in optics and other contexts [28–30]. Replication phenomena are to date regarded as uncontrollable expansions [31], the taming of which represents a fundamental cornerstone yet to be achieved. In sharp contrast with previously known mechanisms [27,31], we show that the spatiotemporal patterns emerging after addition or removal of the entire new rows remain locked. The key ingredients for such transformations are the existence of drift instability and intertwined families of nonlinear waves—rather general features of dissipative systems. These two features simultaneously present in our system enable stepwise self-replications and self-erasures of the multifrequency comb states. Also, our findings are important for the fundamental understanding of pattern transformations and the physics of boundary effects such as stabilization [32] and geometrical frustration [29].

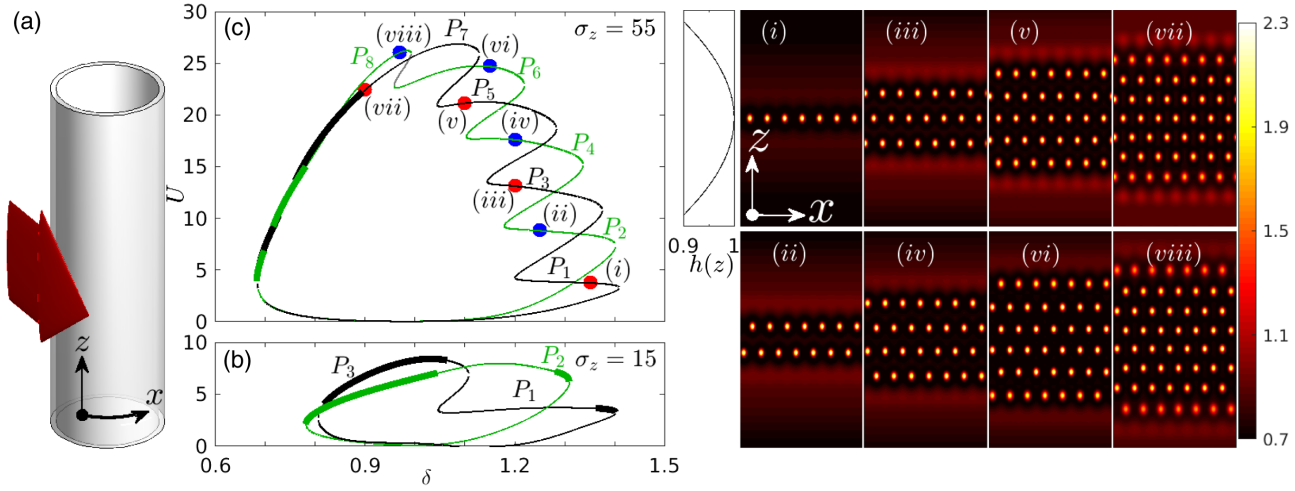

FIG. 1. (a) Sketch of the driven microcylinder. (b),(c) Snaking diagrams of pattern families P_{odd} and P_{even} on the (δ, U) plane for $\sigma_z = 15$ and $\sigma_z = 55$, respectively. Thick traces denote stability. Dots in (c) correspond to the profiles $|\psi(x,z)|$, shown in insets (i)–(viii). Panels' areas span over $x \in [-16, 16)$ (full circumference, $2\pi R$), $z \in [-20, 20]$. Here, $h_0 = \xi(x) = 1$. Scaling: $\Delta\delta = 0.1 \Leftrightarrow 15.6$ MHz, $\sigma_z = 10 \Leftrightarrow 4.9$ mm, $\Delta z = 40 \Leftrightarrow 1.96$ cm, and $h = 1 \Leftrightarrow 46$ mW/mm.

Applying the modal expansion approach [33,34] to a cylindrical microresonator, in which light orbits around its cross section and diffracts along its axis [cf. Fig. 1(a)], yields the generalized damped-driven nonlinear Schrödinger equation [35,36]:

$$\partial_t \psi = \frac{i}{2}[\partial_x^2 + \partial_z^2]\psi - [1 + i\delta]\psi + i|\psi|^2\psi + ih(z,x,t),$$
$$h = h_0 e^{(-z^2/\sigma_z^2)}\xi(x,t), \tag{1}$$

accounting, respectively, for dispersion, diffraction, losses (unity), cavity-laser detuning, Kerr nonlinearity, and pump (see Supplemental Material for model scaling and derivation [37]). Similar models can be used to study comb formation in microbottles [38]. Here, we are primarily concerned with the effects arising in the multifrequency comb states due to a variable pump localization along z (cf. Figs. 1 and 2). However, realistic driving beams will typically couple to a relatively small region of the cylinder's circumference [cf. Fig. 1(a)], which is at rest in the lab frame. Thus, the intracavity field ψ describing the circulating state and the localized pump h have a huge velocity mismatch $\sim c$. In order to take into account the dynamical effects introduced by their relative motion, which could have potentially degraded the practical usefulness of our results [see discussion around Figs. 3 and 4], we will also account for pump localization in x through the function $\xi(x,t) \equiv \sum_{m=-\infty}^{\infty} \exp\left(-[x - m\Delta x - v_g t]^2/\sigma_x^2\right)$, where Δx is the normalized circumference, $x \in [-\Delta x/2, +\Delta x/2)$, and v_g is the normalized group velocity at the pump frequency [37]. Below, we present our results in normalized units, but we provide the link to a reference geometry, consisting of a hollow silica glass cylinder of $R = 200$ μm radius, wall thickness ≈ 1 μm, and quality factor $Q \approx 7.6 \times 10^6$, pumped at $\lambda_p = 1.55$ μm. For the sake of estimates only, we considered the pump as a cw state at $\lambda_p = 1.55$ μm propagating through a rectangular bus waveguide with a gap of 300 nm with the cylinder. The pump values will be translated into power per millimeter along the z direction [37].

The patterns we address exist with anomalous dispersion along x and z, easily attainable with microcylinders. Dispersion along x is readily controlled via the pump's frequency and wall width, and dispersion along z is already anomalous unless modal interactions are specifically engineered [39].

Among all possible pattern solutions of Eq. (1), we focus on hexagonal patterns [40] due to their dominant relative stability [41,42]. Hereafter, P_N denotes hexagonal patterns with N rows along z and fixed separation $x_p = 32/7$ between spots along x [cf. Figs. 1(i)–1(viii)]. Stationary patterns P_N and their stability are computed by imposing $\partial_t \psi = 0$ and assuming uniform in x pump [$\xi(x,t) = 1$]. Figures 1(b) and 1(c) show the existence and stability branches as norm $U \equiv \int_0^{x_p} dx \int_{-\infty}^{\infty} dz |\psi(x,z) - \psi_0(x,z)|^2$ versus cavity detuning for patterns with odd (even) N, P_{odd} (P_{even}), for $\sigma_z = 15$ and $\sigma_z = 55$ (ψ_0 is the background field). Patterns P_1–P_8 are shown in insets (i)–(viii). A salient feature of the $U(\delta)$ branches is the *tilted* snaking structure: Patterns with larger N are stable and exist at lower δ values, while patterns with low N exist at higher δ values, where instabilities typically dominate in 2D [43,44]. The gradual shift in δ of the existence regions is a consequence of the nonuniformity of the pump, h, along z. Indeed, for uniform in z pump, all saddle node bifurcations, i.e., the points where $\partial_\delta U \to \infty$, are (almost) aligned in δ, yielding *straight snaking* [45,46]. While snaking is straightforwardly expected by simple

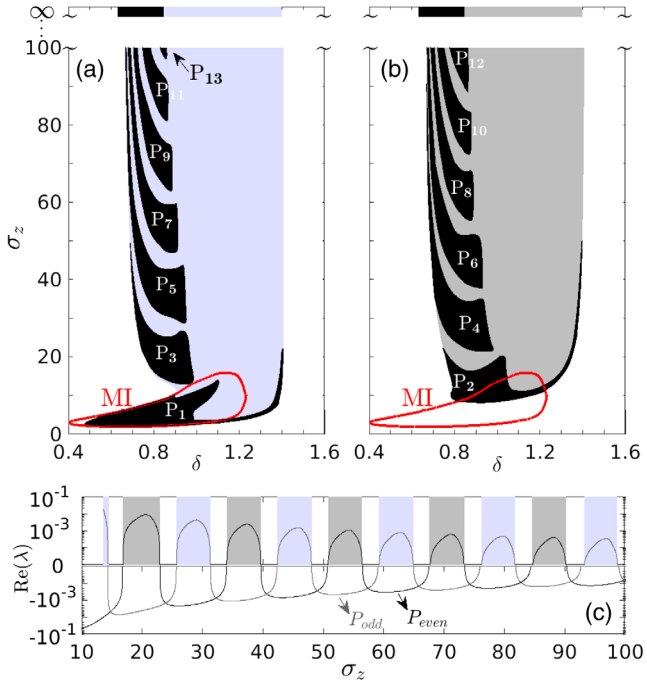

FIG. 2. Existence and stability charts for (a) P_{odd} and (b) P_{even} on the (δ, σ_z) plane [$h_0 = 1$, $\xi(x) = 1$]. Patterns are stable (unstable) within the black (colored) areas. Domains for extended hexagonal pattern ($\sigma_z \to \infty$) are also shown. The red contour encloses the MI area. (c) Drift eigenvalue vs σ_z at $\delta = 0.84$ for the patterns in (a) and (b). Areas in (c) [color matched with (a) and (b)] mark the drift bands for P_{odd} (purple) and P_{even} (gray). Scaling: $\Delta\delta = 0.1 \Leftrightarrow 15.6$ MHz and $\sigma_z = 10 \Leftrightarrow 4.9$ mm.

inspection of the pattern profiles [46], the *tilted snaking* is a rare feature (see, e.g., Ref. [47]) of central importance for this Letter, as it avoids multistability within a pattern family and, thus, enables the pattern self-replicating (-erasure) phenomenon we address below (cf. Ref. [37], Sec. V).

Stability properties of patterns are crucial to elucidate the replication (erasure) process. Thus, all stable domains found in the $U(\delta)$ snaking diagrams [cf. Figs. 1(b) and 1(c)] for $\sigma_z \leq 100$ are presented in Figs. 2(a) and 2(b) for P_{odd} and P_{even}, respectively. Stable patterns exist only in the black areas, while unstable patterns exist within the light colored areas: purple (gray) for P_{odd} (P_{even}). A crucial feature is that, in the interval around $\delta \in [0.75, 0.9]$, the *instability* bands of the two families do not overlap, and, hence, at a given σ_z there exists at least one stable P_N. Additionally, unstable bands are characterized by the sole presence of axial drift (exponential) instability, which induces translation of the pattern along z (upward or downward depending on the particular noise seed). Note that many types of pattern instabilities exist which could heavily distort and potentially destroy them [48]. However, regarding Fig. 2, they are found only for $\delta \gtrsim 0.9$, i.e., outside the interval we address (see [37] for an example of oscillatory instability).

The axial drift instability, crucial for comb replication, arises in our case due to the nonuniform pump field along z. In the uniform pump case, nonlinear states have *neutral* (or Goldstone) internal modes [49] associated to displacements along z, universally characterized by zero growth rate. However, when the pump is modulated in z, the axial translational invariance is broken and the neutral mode eigenvalue deviates from zero to acquire a positive (negative) real part, thus leading to patterns that are unstable (stable) to drift along z (see, e.g., discussions in Refs. [50,51]). In our case, and consistent with formal

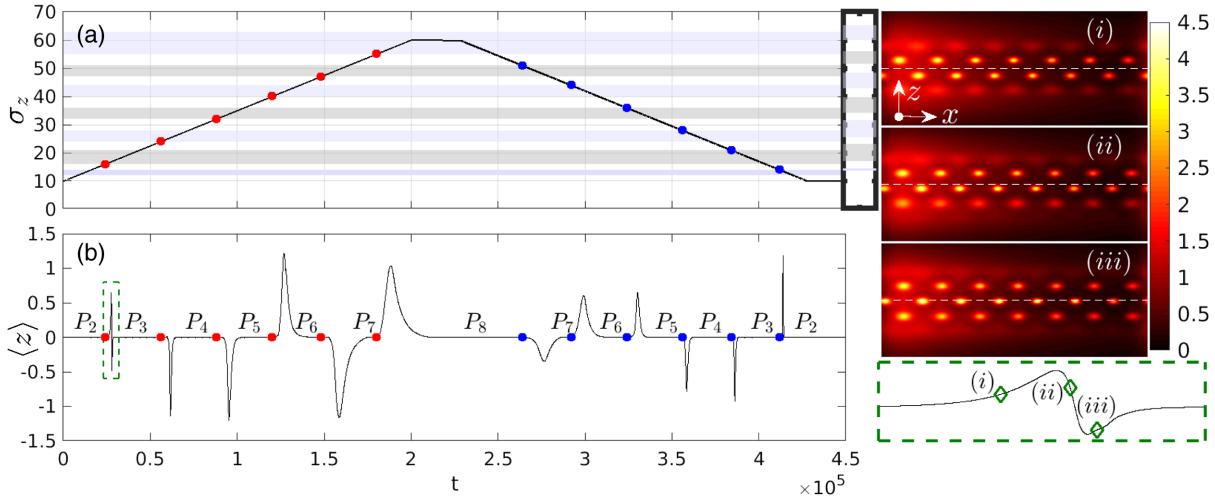

FIG. 3. Pattern self-replication and self-erasure under the two-dimensional localization of the pump, $h_0 \approx 9$, $\sigma_x = 2$, and varying $\sigma_z(t)$ with $\delta = 0.84$. (a),(b) Evolution of σ_z and center of mass. Dots in (a) and (b) mark the entrance into the drift-instability regions for P_{odd} (purple) and P_{even} (gray). The inset in (a) shows the drift bands for $\xi = 1$ [cf. Fig. 2(c)]. The dashed green rectangle enlarges the $P_2 \to P_3$ transition from (b), while distributions $|\psi(x,z)|^2$ correspond to labels (i)–(iii). Axes of panels (i)–(iii): $x \in [-16, 16)$ (full circumference), $z \in [-12, 12]$. Scaling: $\sigma_z = 10 \Leftrightarrow 4.9$ mm, $\langle z \rangle = 1 \Leftrightarrow 490$ μm, $t = 1 \Leftrightarrow 10^3$ round-trips, $\tau \approx 6.4$ ps, total propagated time ~2.9 ms, $\Delta z = 24 \Leftrightarrow 1.2$ cm, $\sigma_x = 2 \Leftrightarrow \pi R/8$, and $h_0 = 9 \Leftrightarrow 3$ W/mm.

theorems for conservative systems [51], the *perturbed* neutral eigenvalue remains real but oscillates around zero with σ_z, as shown in Fig. 2(c). The regions where $\mathrm{Re}(\lambda) > 0$ correspond to drift instabilities for P_{odd} (purple) and P_{even} (gray) pattern families. The amplitude of oscillations of $\mathrm{Re}(\lambda)$ (plotted in log scale) decreases very fast as σ_z increases, because the system tends to recover its axial translational invariance and drift-free dynamics. In the flat pump limit, multicomb states become infinitely extended hexagonal patterns, whose existence and stability domain is shown in Figs. 2(a) and 2(b).

In addition to the above stability properties, we highlight the presence of a modulation instability (MI) region, encircled in Figs. 2(a) and 2(b) by the red line, where stable patterns $P_{1,2}$ are easily excitable by the cw pump. The simultaneous presence of MI and alternating drift instability bands for our specific choice of the pump amplitude $h_0 = 1$ is essential for the dynamical transformations between P_{odd} and P_{even} families and could not be anticipated *a priori*. Indeed, for $h_0 > 1$ the MI region expands, but the stability domains shrink, and vice versa for $h_0 < 1$ (not shown).

A sequence of stepwise pattern transitions of the type $P_N \to P_{N+1}$ (P_{N-1}) leading to deterministic self-replication (-erasure) are shown in Fig. 3. Simulation of Eq. (1) was initiated with the P_2 pattern obtained at $\delta = 0.84$, $\sigma_z = 10$, $\sigma_x = 2$, and $h_0 \approx 9$. Here we take into account that in the experiment the pump profile is typically localized in x; hence, pump amplitude h_0 was adjusted to closely correspond to the dynamics observed for uniform in x pump. As time goes on, the pump width σ_z is gradually increased up to 60, where excitation of the stable P_8 pattern is observed, and then decreased back down to 10, leading to restoration of the stable P_2 pattern [see Figs. 3(a) and 3(b)] (note that the total pump power increases with σ_z, as h_0 is constant). Transitions are triggered at the times (marked by red and blue dots) where varying σ_z drives P_N outside its stability region and into the region where it becomes unstable and starts to drift spontaneously upward or downward in z [see gray (purple) shaded regions for P_{even} (P_{odd}) families]. When σ_z increases (decreases), the drift induces the transition $P_N \to P_{N+1}$ (P_{N-1}), as expected from Figs. 2(a) and 2(b). While axially *locked* patterns have zero average axial position [cf. Figs. 1(i)–1(vii)], $\langle z \rangle \equiv \int_0^{x_p} dx \int_\infty^\infty z dz |\psi - \psi_0|^2 / U \equiv 0$, the z-drifting transient states do not, and thus the transitions $P_N \to P_{N\pm1}$ are characterized by pronounced peaks in $\langle z \rangle$ vs t, apparent in Fig. 3(b). These peaks show that transitions at larger σ_z (larger N) take more time, in agreement with the fast decrease of the growth rate $\mathrm{Re}(\lambda)$ with pump width [Fig. 2(c)] (see, e.g., Ref. [52] for a discussion on drift speeds). Details of the transition $P_2 \to P_3$ are illustrated within the dashed rectangle in Fig. 3(b), and selected transient pattern profiles are shown in Figs. 3(i)–3(iii). We emphasize that *coexistence of a drift unstable family and a stable one is crucial* for the reported effects. Fortunately, stationary pattern states with nonzero average position, $\langle z \rangle \neq 0$, were not found to exist within the investigated parameter space (cf. Ref. [37], Sec. V). States of this sort may exist with modulated background, and, if they exist, they could have frustrated comb replications.

We note that the drift instability bands in Fig. 3(a) do not coincide exactly with those in Fig. 2(c), plotted also as an inset in Fig. 3(a), for clarity. This is because patterns in Figs. 1 and 2 were calculated for unit $\xi(x,t)$ (flat in x pump), while the propagation takes into account the x localization of $\xi(x,t)$. The impact of $\xi(x,t)$, representing a nonautonomous perturbation, is well tested in 1D, but it is not in 2D. Hence, our results show the robustness of the comb replication effect in the regime where the steady state calculations of Figs. 1 and 2 cannot be easily done, a feature that is crucial for the experimental demonstration of the phenomenon. We stress that other case-specific autonomous perturbations arising from linear dispersion [53–61] and moderate Raman effect [62–65] are perfectly compatible with robust nonlinear states and, for the sake of generality, are not considered here.

Figures 4(a)–4(c) show multicomb spectra in the (k_x, z) plane of patterns P_1 (a), P_3 (b), and P_8 (c), obtained under the same conditions as those in Fig. 3 at constant σ_z (see labels). One-dimensional spectra at specific z values are shown in Figs. 4(d)–4(f). Because patterns include seven periods in the x direction [cf. Figs. 3(i)–3(iii)], all spectra feature high-amplitude peaks separated by seven FSRs. The other much weaker resonances appear due to x dependence of $\xi(x,t)$, as noted previously [66], and tend to zero in the case $\xi(x,t) = 1$ [37]. In the geometry considered above, the spectra in Figs. 4(e) and 4(f) span from 1.35 to 1.82 μm,

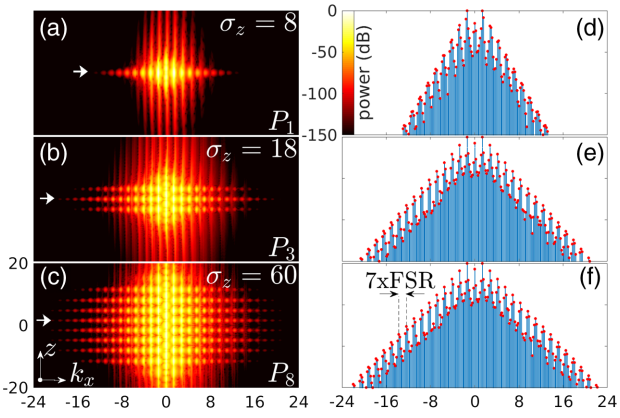

FIG. 4. Robust multicomb spectra for (a) P_1, (b) P_3, and (c) P_8 (σ_z in labels) for the same parameters as Fig. 3. (d)–(f) Spectra at the selected z positions (white arrows) in (a)–(c), respectively. All power levels are in the range $[-150, 0]$ dB. The background field $\psi_0(x,z)$ was subtracted prior to Fourier transforms. Scaling: $\Delta\kappa_x = 1 \Leftrightarrow 1/40\mu\mathrm{m}^{-1}$. At $\lambda_p = 1.55\,\mu$m, $\Delta\kappa_x = 48 \Leftrightarrow \lambda_0 \in [1.35, 1.82]$ μm. $\Delta z = 40 \Leftrightarrow 1.96$ cm.

corresponding to an equivalent duration of individual solitons of about ∼200 fs.

In closing, we stress that the phenomenon described here reveals a mechanism that replicates and erases frequency combs along the axis of a cylindrical microresonator in a stepwise deterministic manner, affording a robust way to manipulate multifrequency combs states in the form of spatiotemporal patterns. The frequency combs tend to be exact copies of each other and are inherently synchronized. These two features are promising for important applications such as spectroscopy, communications, rf links, and imaging. This effect is based on a fundamental drift instability that dynamically connects pattern families with odd and even numbers of rows (or combs) while preserving the overall symmetry. Emerging patterns via these transformations are locked and robust. Our results also bring a fundamental understanding of the mechanism of pattern transformations, a phenomenon of major importance in the general context of nonlinear waves in dissipative media.

This work was partially supported by the Government of Spain (Grants No. IJCI-2016-27752, No. MTM2016-75963-P, and No. FIS2015-71559-P; Severo Ochoa CEX2019-000910-S); Generalitat de Catalunya; Centres de Recerca de Catalunya; Fundació Cellex; and Fundació Mir-Puig.

*carmien@upvnet.upv.es

[1] T. Herr, V. Brasch, J. D. Jost, C. Y. Wang, N. M. Kondratiev, M. L. Gorodetsky, and T. J. Kippenberg, Temporal solitons in optical microresonators, Nat. Photonics **8**, 145 (2014).

[2] X. Yi, Q. F. Yang, K. Y. Yang, and K. Vahala, Active capture and stabilization of temporal solitons in microresonators, Opt. Lett. **41**, 2037 (2016).

[3] V. Brasch, M. Geiselmann, M. H. Pfeiffer, and T. J. Kippenberg, Bringing short-lived dissipative Kerr soliton states in microresonators into a steady state, Opt. Express **24**, 29312 (2016).

[4] D. T. Spencer *et al.*, An optical-frequency synthesizer using integrated photonics, Nature (London) **557**, 81 (2018).

[5] M.-G. Suh, Q.-F. Yang, K. Y. Yang, X. Yi, and K. J. Vahala, Microresonator soliton dual-comb spectroscopy, Science **354**, 600 (2016).

[6] P. Marin-Palomo, J. N. Kemal, M. Karpov, A. Kordts, J. Pfeifle, M. H. P. Pfeiffer, P. Trocha, S. Wolf, V. Brasch, M. H. Anderson, R. Rosenberger, K. Vijayan, W. Freude, T. J. Kippenberg, and C. Koos, Microresonator-based solitons for massively parallel coherent optical communications, Nature (London) **546**, 274 (2017).

[7] M.-G. Suh and K. J. Vahala, Soliton microcomb range measurement, Science **359**, 884 (2018).

[8] A. L. Gaeta, M. Lipson, and T. J. Kippenberg, Photonic-chip-based frequency combs, Nat. Photonics **13**, 158 (2019).

[9] T. J. Kippenberg, A. L. Gaeta, M. Lipson, and M. L. Gorodetsky, Dissipative Kerr solitons in optical microresonators, Science **361**, eaan8083 (2018).

[10] A. Pasquazi *et al.*, Micro-combs: A novel generation of optical sources, Phys. Rep. **729**, 1 (2018).

[11] D. C. Cole, E. S. Lamb, P. DelHaye, S. A. Diddams, and S. B. Papp, Soliton crystals in Kerr resonators, Nat. Photonics **11**, 671 (2017).

[12] M. Karpov, M. H. P. Pfeiffer, H. Guo, W. Weng, J. Liu, and T. J. Kippenberg, Dynamics of soliton crystals in optical microresonators, Nat. Phys. **15**, 1071 (2019).

[13] Z. Qi, S. Wang G, J. Jaramillo-Villegas, M. Qi, A. M. Weiner, G. DAguanno, T. F. Carrythers, and C. R. Menyuk, Dissipative cnoidal waves (Turing rolls) and the soliton limit in microring resonators, Optica **6**, 1220 (2019).

[14] H. Bao, L. Olivieri, M. Rowley, S. T. Chu, B. E. Little, R. Morandotti, D. J. Moss, J. S. T. Gongora, M. Peccianti, and A. Pasquazi, Turing patterns in a fiber laser with a nested microresonator: Robust and controllable microcomb generation, Phys. Rev. Research **2**, 023395 (2020).

[15] J. Szabados, D. N. Puzyrev, Y. Minet, L. Reis, K. Buse, A. Villois, D. V. Skryabin, and I. Breunig, Frequency Comb Generation Via Cascaded Second-Order Nonlinearities in Microresonators, Phys. Rev. Lett. **124**, 203902 (2020).

[16] C. Godey, I. V. Balakireva, A. Coillet, and Y. K. Chembo, Stability analysis of the spatiotemporal Lugiato-Lefever model for Kerr optical frequency combs in the anomalous and normal dispersion regimes, Phys. Rev. A **89**, 063814 (2014).

[17] P. Parra-Rivas, D. Gomila, L. Gelens, and E. Knobloch, Bifurcation structure of periodic patterns in the Lugiato-Lefever equation with anomalous dispersion, Phys. Rev. E **98**, 042212 (2018).

[18] N. Picqué and T. W. Hänsch, Frequency comb spectroscopy, Nat. Photonics **13**, 146 (2019).

[19] N. G. Pavlov, G. Lihachev, S. Koptyaev, E. Lucas, M. Karpov, N. M. Kondratiev, I. A. Bilenko, T. J. Kippenberg, and M. L. Gorodetsky, Soliton dual frequency combs in crystalline microresonators, Opt. Lett. **42**, 514 (2017).

[20] J. K. Jang, A. Klenner, X. Ji, Y. Okawachi, M. Lipson, and A. L. Gaeta, Synchronization of coupled optical microresonators, Nat. Photonics **12**, 688 (2018).

[21] C. Bao, M.-G. Suh, and K. Vahala, Microresonator soliton dual-comb imaging, Optica **6**, 1110 (2019).

[22] S. B. Papp, P. DelHaye, and S. A. Diddams, Mechanical Control of a Microrod-Resonator Optical Frequency Comb, Phys. Rev. X **3**, 031003 (2013).

[23] T. Kipp, H. Welsch, C. Strelow, C. Heyn, and D. Heitmann, Optical Modes in Semiconductor Microtube Ring Resonators, Phys. Rev. Lett. **96**, 077403 (2006).

[24] K. J. Lee, W. D. McCormick, J. E. Pearson, and H. L. Swinney, Experimental observation of self-replicating spots in a reaction-diffusion system, Nature (London) **369**, 215 (1994).

[25] J. E. Pearson, Complex patterns in a simple system, Science **261**, 189 (1993).

[26] W. N. Reynolds, J. E. Pearson, and S. Ponce-Dawson, Dynamics of Self-Replicating Patterns in Reaction Diffusion Systems, Phys. Rev. Lett. **72**, 2797 (1994).

[27] E. Bodenschatz, J. R. de Bruyn, G. Ahlers, and D. S. Cannell, Transitions Between Patterns in Thermal Convection, Phys. Rev. Lett. **67**, 3078 (1991).

[28] A. S. Mikhailov and K. Showalter, Control of waves, patterns and turbulence in chemical systems, Phys. Rep. **425**, 79 (2006).
[29] S. Residori, Patterns, fronts and structures in a liquid-crystal-light-valve with optical feedback, Phys. Rep. **416**, 201 (2005).
[30] F. T. Arecchi, S. Boccaletti, and P. Ramazza, Pattern formation and competition in nonlinear optics, Phys. Rep. **318**, 1 (1999).
[31] J. Burke and E. Knobloch, Homoclinic snaking: Structure and stability, Chaos **17**, 037102 (2007).
[32] G. Kozyreff, P. Assemat, and S. J. Chapman, Influence of Boundaries on Localized Patterns, Phys. Rev. Lett. **103**, 164501 (2009).
[33] Y. K. Chembo and N. Yu, Modal expansion approach to optical-frequency-comb generation with monolithic whispering-gallery-mode resonators, Phys. Rev. A **82**, 033801 (2010).
[34] Y. K. Chembo and C. R. Menyuk, Spatiotemporal Lugiato-Lefever formalism for Kerr-comb generation in whispering-gallery-mode resonators, Phys. Rev. A **87**, 053852 (2013).
[35] L. A. Lugiato and R. Lefever, Spatial Dissipative Structures in Passive Optical Systems, Phys. Rev. Lett. **58**, 2209 (1987).
[36] M. Haelterman, S. Trillo, and S. Wabnitz, Dissipative modulation instability in a nonlinear dispersive ring cavity, Opt. Commun. **91**, 401 (1992).
[37] See Supplemental Material at http://link.aps.org/supplemental/10.1103/PhysRevLett.126.063903 for a model derivation outline, scaling, estimates of realistic cavity geometries and pump power, impact of a localized pump on spectra, oscillatory dynamics of patterns, and branches of patterns as norm vs pump width.
[38] Y. V. Kartashov, M. L. Gorodetsky, A Kudlinski, and D. V. Skryabin, Two-dimensional nonlinear modes and frequency combs in bottle microresonators, Opt. Lett. **43**, 2680 (2018).
[39] M. Ibanescu, S. G. Johnson, D. Roundy, C. Luo, Y. Fink, and J. D. Joannopoulos, Anomalous Dispersion Relations by Symmetry Breaking in Axially Uniform Waveguides, Phys. Rev. Lett. **92**, 063903 (2004).
[40] W. J. Firth, A. J. Scroggie, G. S. McDonald, and L. A. Lugiato, Hexagonal patterns in optical bistability, Phys. Rev. A **46**, R3609 (1992).
[41] A. J. Scroggie, W. J. Firth, G. S. McDonald, M. Tlidi, R. Lefever, and L. A. Lugiato, Pattern formation in a passive Kerr cavity, Chaos Solitons Fractals **4**, 1323 (1994).
[42] M. Tlidi, R. Lefever, and P. Mandel, Pattern selection in optical bistability, Quantum Semiclass. Opt. **8**, 931 (1996).
[43] D. Gomila, A. J. Scorggie, and W. J. Firth, Bifurcation structure of dissipative solitons, Physica (Amsterdam) **227D**, 70 (2007).
[44] W. J. Firth, G. K. Harkness, A. Lord, J. M. McSloy, D. Gomila, and P. Colet, Dynamical properties of two-dimensional Kerr cavity solitons, J. Opt. Soc. Am. B **19**, 747 (2002).
[45] P. Parra-Rivas, D. Gomila, L. Gelens, and E. Knobloch, Bifurcation structure of localized states in the Lugiato-Lefever equation with anomalous dispersion, Phys. Rev. E **97**, 042204 (2018).
[46] D Avitabile, D. J. B. Lloyd, J. Burke, E. Knobloch, and B. Sandstede, To snake or not to snake in the Planar SwiftHohenberg equation, SIAM J. Appl. Dyn. Syst. **9**, 704 (2010).
[47] W. J. Firth, L. Columbo, and T. Maggipinto, On homoclinic snaking in optical systems, Chaos **17**, 037115 (2007).
[48] D. Gomila and P. Colet, Dynamics of hexagonal patterns in a self-focusing Kerr cavity, Phys. Rev. E **76**, 016217 (2007).
[49] D. V. Skryabin, Energy of the soliton internal modes and broken symmetries in nonlinear optics, J. Opt. Soc. Am. B **19**, 529 (2002).
[50] A. J. Scroggie, D. Gomila, W. J. Firth, and G.-L. Oppo, Spontaneous and induced motion of optical patterns, Appl. Phys. B **81**, 963 (2005).
[51] Y. Sivan, G. Fibich, B. Ilan, and M. I. Weinstein, Qualitative and quantitative analysis of stability and instability dynamics of positive lattice solitons, Phys. Rev. E **78**, 046602 (2008).
[52] T. Maggipinto, M. Brambilla, G. K. Harkness, and W. J. Firth, Cavity solitons in semiconductor microresonators: Existence, stability, and dynamical properties, Phys. Rev. E **62**, 8726 (2000).
[53] C. Milián, Y. V. Kartashov, D. V. Skryabin, and L. Torner, Clusters of Cavity Solitons Bounded by Conical Radiation, Phys. Rev. Lett. **121**, 103903 (2018).
[54] M. R. E. Lamont, Y. Okawachi, and A. L. Gaeta, Route to stabilized ultrabroadband microresonator-based frequency combs, Opt. Lett. **38**, 3478 (2013).
[55] S. Coen, H. G. Randle, T. Sylvestre, and M. Erkintalo, Modeling of octave-spanning Kerr frequency combs using a generalized mean-field Lugiato-Lefever model, Opt. Lett. **38**, 37 (2013).
[56] C. Milián and D. Skryabin, Soliton families and resonant radiation in a micro-ring resonator near zero group-velocity dispersion, Opt. Express **22**, 3732 (2014).
[57] P. Parra-Rivas, D. Gomila, F. Leo, S. Coen, and L. Gelens, Third-order chromatic dispersion stabilizes Kerr frequency combs, Opt. Lett. **39**, 2971 (2014).
[58] D. V. Skryabin and Y. V. Kartashov, Self-locking of the frequency comb repetition rate in microring resonators with higher order dispersions, Opt. Express **25**, 27442 (2017).
[59] J. H. Talla Mbé, C. Milián, and Y. K. Chembo, Existence and switching behavior of bright and dark Kerr solitons in whispering-gallery mode resonators with zero group-velocity dispersion, Eur. Phys. J. D **71**, 196 (2017).
[60] V. Brasch, M. Geiselmann, T. Herr, G. Lihachev, M. H. P. Pfeiffer, M. L. Gorodetsky, and T. J. Kippenberg, Photonic chipbased optical frequency comb using soliton Cherenkov radiation, Science **351**, 357 (2016).
[61] X. Yi, Q.-F. Yang, X. Zhang, K. Y. Yang, X. Li, and K. Vahala, Single-mode dispersive waves and soliton microcomb dynamics, Nat. Commun. **8**, 14869 (2017).
[62] C. Milián, A. V. Gorbach, M. Taki, A. V. Yulin, and D. V. Skryabin, Solitons and frequency combs in silica microring resonators: Interplay of the Raman and higher-order dispersion effects, Phys. Rev. A **92**, 033851 (2015).

[63] M. Karpov, H. Guo, A. Kordts, V. Brasch, M. H. P. Pfeiffer, M. Zervas, M. Geiselmann, and T. J. Kippenberg, Raman Self-Frequency Shift of Dissipative Kerr Solitons in an Optical Microresonator, Phys. Rev. Lett. **116**, 103902 (2016).

[64] Q.-F. Yang, X. Yi, K. Y. Yang, and K. Vahala, Stokes solitons in optical microcavities, Nat. Phys. **13**, 53 (2017).

[65] M. Yu, Y. Okawachi, R. Cheng, C. Wang, M. Zhang, A. L. Gaeta, and Marko Lonar, Raman lasing and soliton mode-locking in lithium niobate microresonators, Light Sci. Appl. **9**, 9 (2020).

[66] Y. V. Kartashov, O. Alexander, and D. V. Skryabin, Multistability and coexisting soliton combs in ring resonators: The Lugiato-Lefever approach, Opt. Express **25**, 11550 (2017).